Supplementary material for "The CESM2 Single Forcing Large Ensemble and Comparison to CESM1: Implications for Experimental Design"

Isla R. Simpson[a] , Nan Rosenbloom[a] , Gokhan Danabasoglu[a] , Clara Deser[a] , Stephen G. Yeager[a] ,

Christina S. McCluskey[a] , Ryohei Yamaguchi[b] , Jean-Francois Lamarque[a] , Simone Tilmes[c] ,

Michael J. Mills[c] , Keith B. Rodgers[d,e]

[a] *Climate and Global Dynamics Laboratory, National Center for Atmospheric Research, Boulder, Colorado*

[b] *Japan Agency for Marine-Earth Science and Technology, Yokosuka, Japan*

[c] *Atmospheric Chemistry Observations and Modelling Laboratory, National Center for Atmospheric Research, Boulder, Colorado*

[d] *Center for Climate Physics, Insitute for Basic Science, Busan, South Korea*

[e] *Pusan National University, Busan, South Korea*

Corresponding author: Isla Simpson, islas@ucar.edu
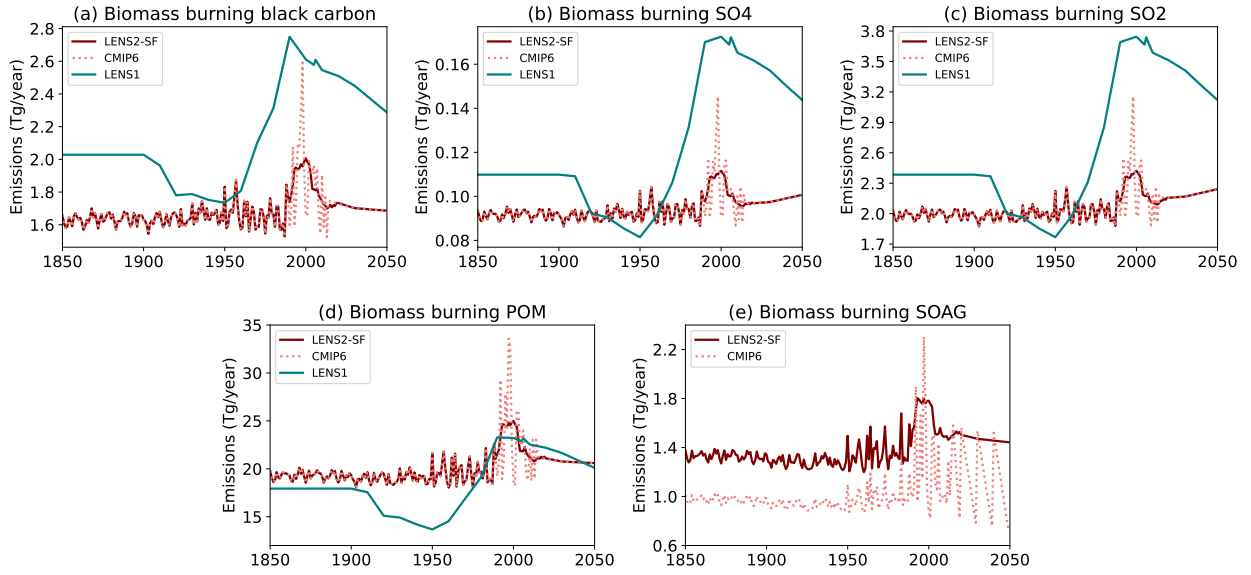
FIG. 1. A comparison of biomass burning emissions of (a) black carbon, (b) SO_4, (c) SO_2, (d) Primary Organic Matter (POM), and (e) Secondary Organic Aerosol precursor Gases (SOAG) between LENS1 (teal), the CESM2 single forcing large ensemble (maroon solid) and the CMIP6 historical and SSP3-7.0 biomass burning emissions (dotted salmon). Note that LENS1 is not shown for SOAG as it was not possible to divide SOAG emissions up into the different components in the same way in CESM1. Note also that for SOAG, the differences in emissions between CMIP6 and the single forcing large ensemble reflects a correction to the CESM2 SOAG emissions between the first and second 50 members of LENS2 (Rodgers et al. 2021).
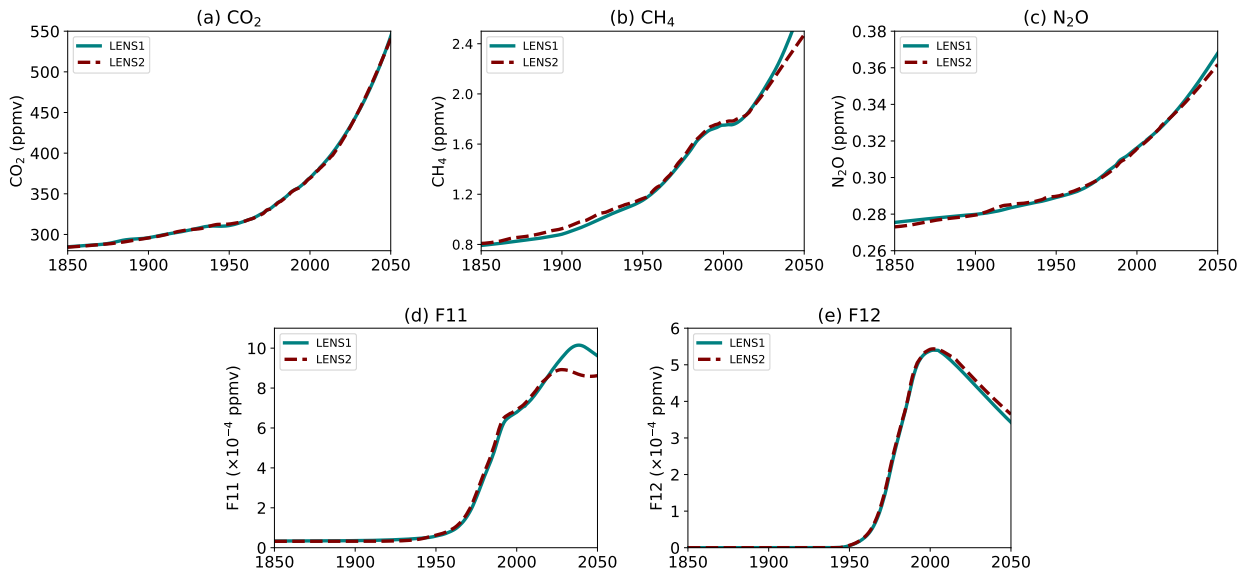

FIG. 2. A comparison of global mean greenhouse gas concentrations between the LENS1 (solid teal) and LENS2 (dashed maroon). (a) CO_2, (b) CH_4, (c) N_2O, (d) F11, (e) F12.
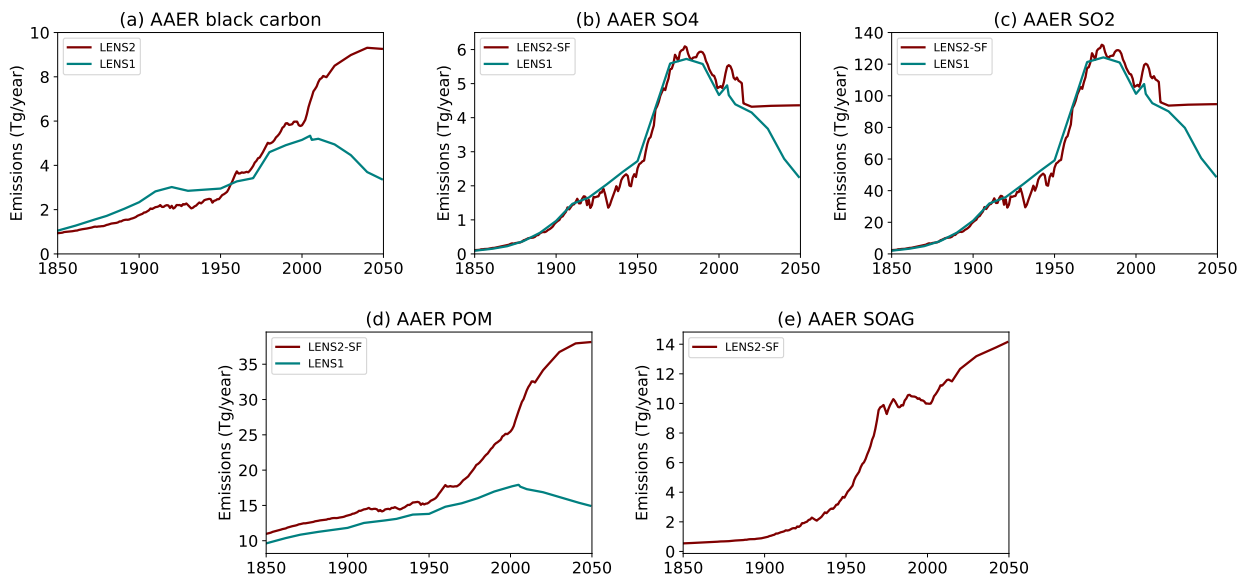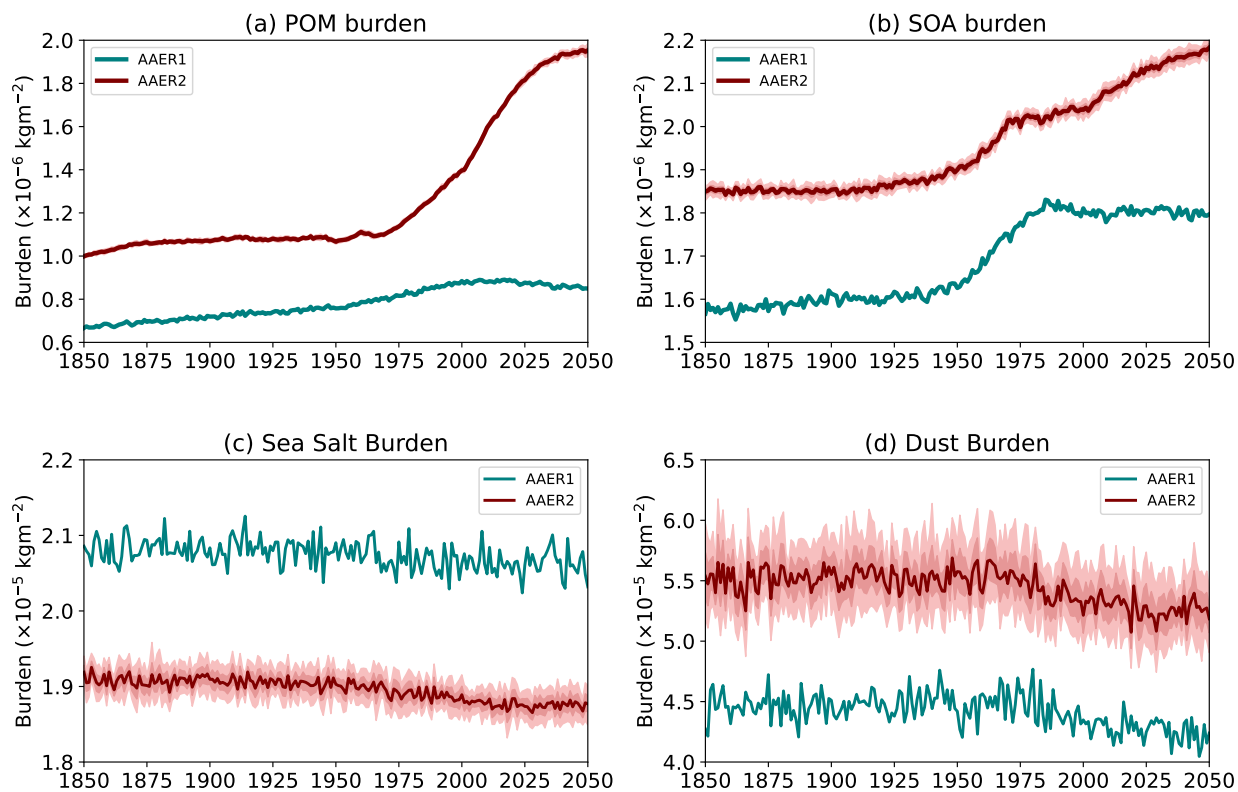
2

FIG. 3. A comparison of anthropogenic aerosol emissions between LENS1 (teal) and LENS2 (maroon): (a) Black Carbon, (b) SO$_4$, (c) SO$_2$, (d) POM, and (e) SOAG.

FIG. 4. Globally averaged aerosol burden in the AAER1 (teal) and AAER2 (maroon) experiments. The uncertainty range estimated by bootstrapping the AAER2 ensemble members with replacement is shown for the 15 member AAER2 ensemble in the dark shading and for a 3 member ensemble in light shading.
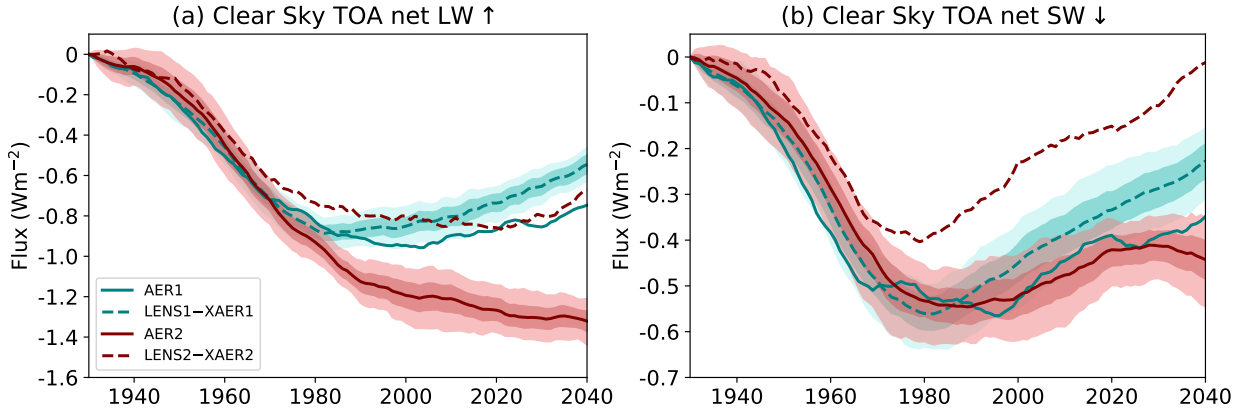
3

FIG. 5. 21 year running means of annual mean global mean flux anomalies relative to 1920-1940 for CESM1 and CESM2 aerosol forced trends. (a) Clear sky top of atmosphere net longwave upwards radiation and (b) clear sky top of atmosphere net shortwave downwards radiation.
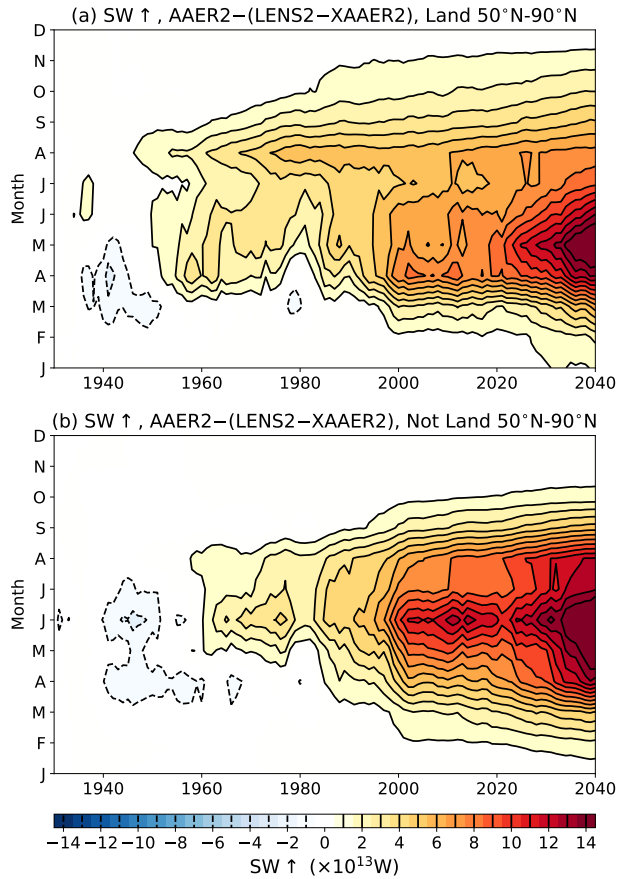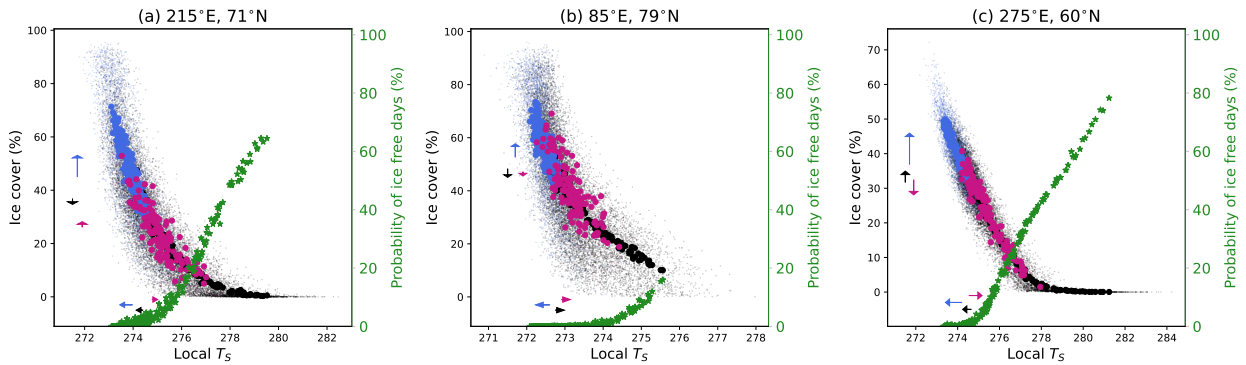

FIG. 6. Differences in surface upward shortwave (21 year running mean anomalies from 1920-1940) between AAER2 and LENS2−XAAER2 for regions north of 50°N integrated over (a) land and (b) not land regions.

FIG. 7. Evolution of sea ice cover as a function of local near surface air temperature (T_s) for three points: 215°E, 71°N to the North of Alaska; 85°E, 79°N to the southwest of Svalbard ; and, 275°E, 60°N in Hudson Bay. Dots show the JJA seasonal mean percentage of the grid point covered by sea ice versus local T_s. Small dots show the individual seasons for all members and all years and large dots show the ensemble means for each year. Blue = AAER2, pink = XAAER2 and black = LENS2 (LENS2 is shown out to 2100). The green stars (right axis) show the probability of sea ice free days in the JJA season assessed for each year by pooling together all members from either LENS2 or AAER2 (XAAER2 is now shown for this metric given its smaller ensemble size). The start point of each arrow shows the ensemble mean 1920-1940 average value and the end point shows the ensemble mean 1960-1980 average. The overall change in AAER2 is simply quantified by the length and direction of the blue arrow while the magnitude of the change in LENS2−XAAER2 is given by summing up the length of the black and pink arrows when they are in opposite direction or subtracting the length of the pink arrow from the length of the black arrow when they are in the same direction.
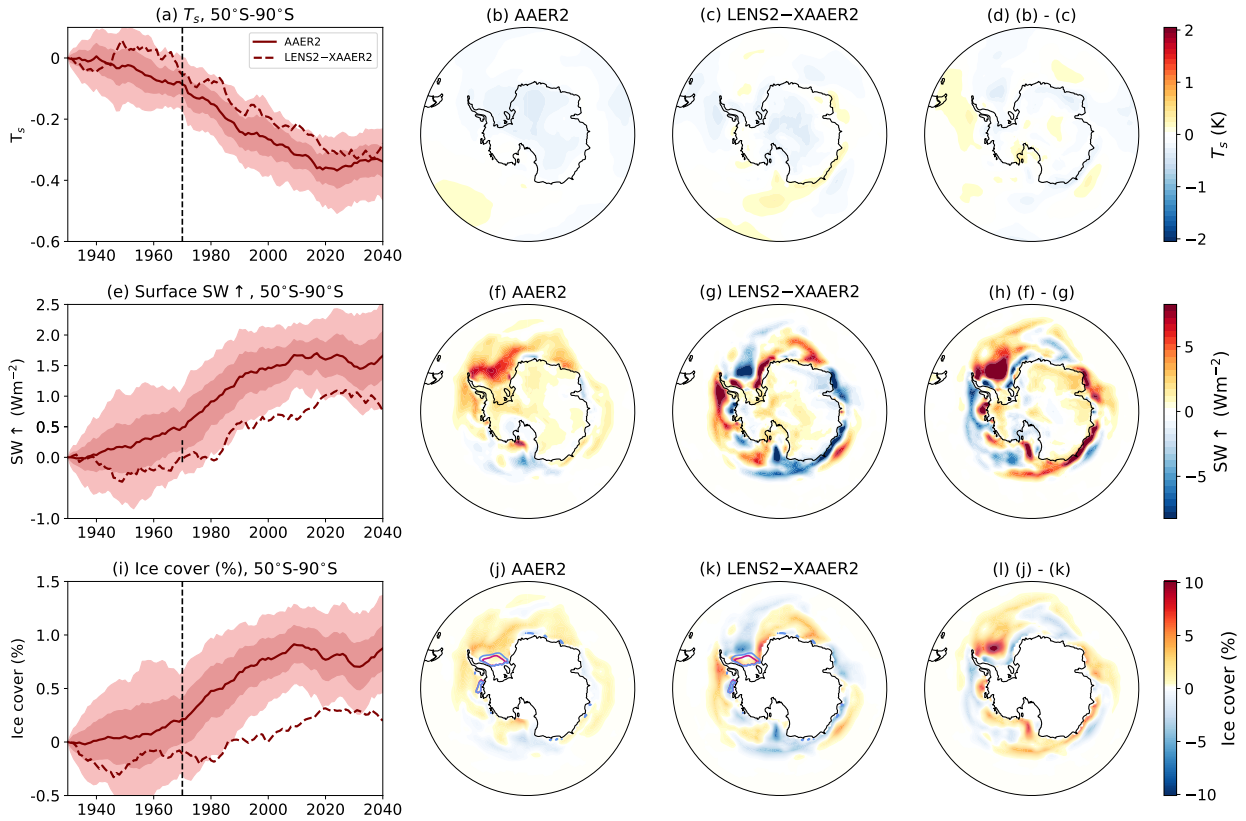
FIG. 8. (a)-(d) show DJF averaged near surface air temperature. (a) shows time series of 50°S-90°S average anomalies from 1920-1940. (b) Shows the anomalies for 1960-1980 for AAER2, (c) shows the anomalies for 1960-1980 for LENS2−XAAER2 and (d) shows the difference in anomalies between AAER2 and LENS2−XAAER2. (e)-(h) are as (a)-(d) but for surface upward shortwave radiation and (i)-(l) are as (a)-(d) but for the average percentage cover of sea ice in each grid point. The blue and purple contours in (j) and (k) show the 80% ice coverage contours for 1920 to 1940 of AAER2 and 1960 to 1980 of XAAER2 respectively.
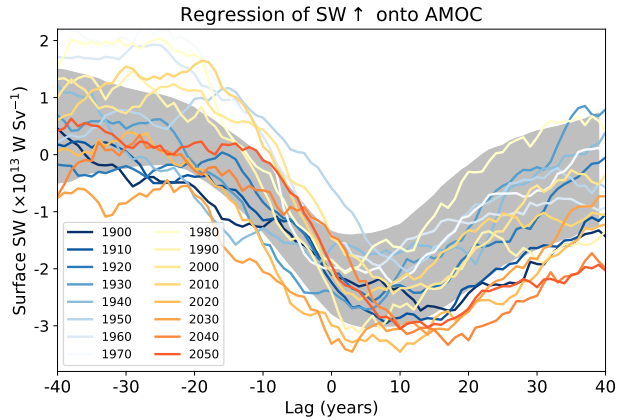
FIG. 9. Regression of globally integrated surface upwards shortwave onto AMOC (defined as the maximum meridional stream function below 500m at 45°N) using 21-year running means. The gray shaded range shows the 95% confidence interval of bootstrap samples generated from the CESM2 piControl by randomly sampling (with replacement) chunks of length 200 years and concatenating them to make 1000, 1600 year time series and recalculating the regression of globally integrated upwards shortwave onto AMOC 1000 times. The colored line shows the lagged regression of globally integrated upward shortwave onto AMOC across the 50 ensemble members of LENS2 using anomalies from the LENS2 ensemble mean for a range of 21 year periods centered between 1900 and 2050. The uncertainty on the LENS2 regressions is much larger than that for the piControl since only 50 21-year means are contributing to the regression but still the majority of colored lines lie within the piControl uncertainty. There is no clear monotonic change in the regression behavior at least out to about 2000. The 21st century years tend to be on the most negative end of the distribution - whether this is a climate change signal or uncertainty due to the small sample size is unclear, but overall this suggests that any time evolution of the link between AMOC and globally integrated surface upward shortwave is probably captured reasonably well by the procedure to produce the uncertainty range in Fig 11 of the main text.
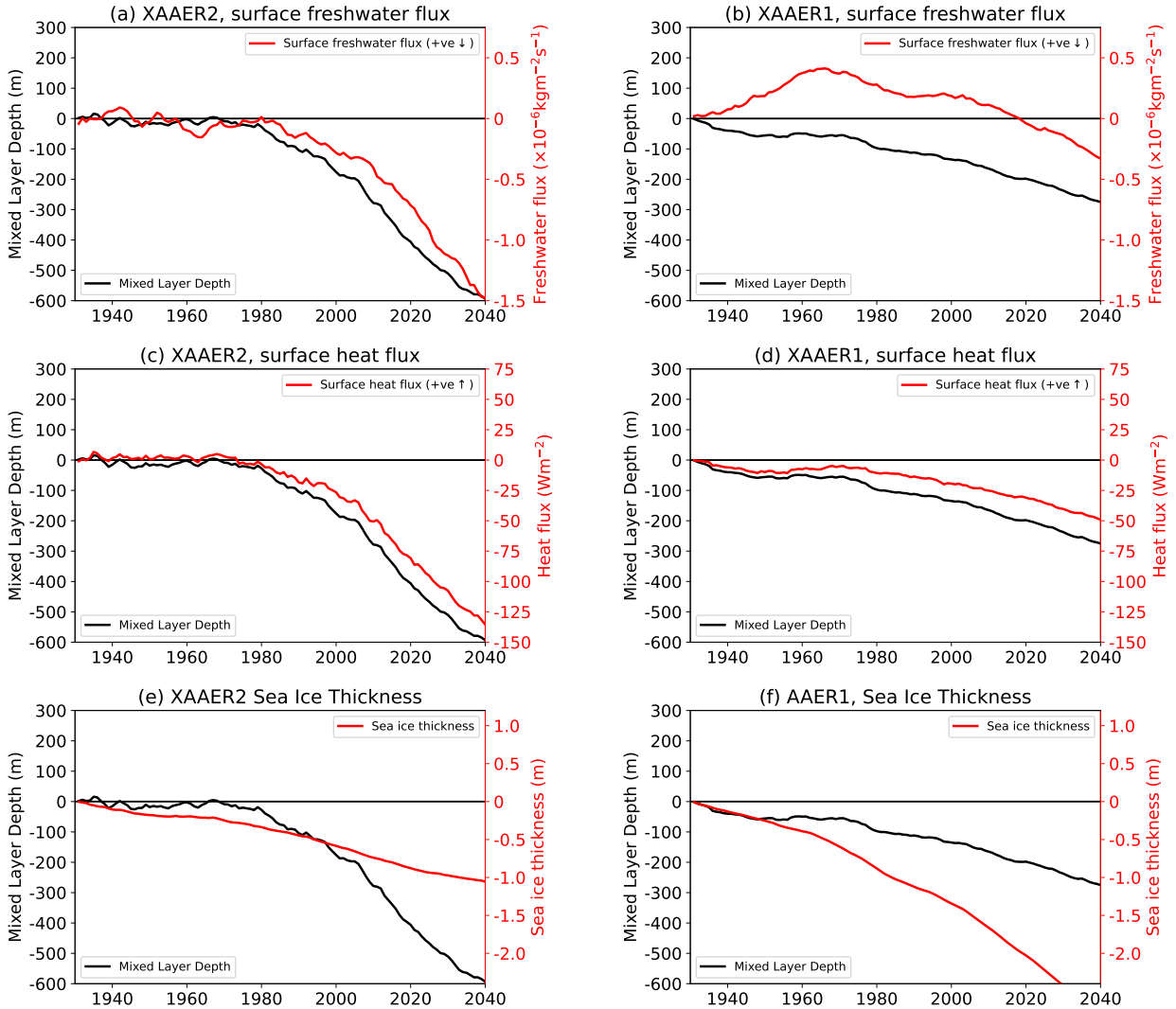
Fig. 10. Time series of 21 year running mean anomalies from 1920-1940. Left shows the XAAER2 simulation and right shows the XAAER1 simulation. The black lines (left axes) show the March mixed layer depth averaged over the Labrador Sea (300°E-315°E, 53°N-65°N) and is the same in each row. The red lines (right axes) show DJFM averages of potential drivers of AMOC decline with the year corresponding to the year of March in the DJFM average. Top shows the surface freshwater flux averaged over the Labrador Sea, middle shows the surface heat flux averaged over the Labrador Sea, and bottom shows the sea ice thickness averaged over 220°E-360°E, 70°N-90°N (the same as shown in Fig. 12a of the main text). (a) and (b) show that the net surface freshwater flux declines in CESM2 so it cannot be a driver of the AMOC decline in CESM2, nor can differences in the net surface freshwater flux explain the greater AMOC decline in CESM2 because there is a greater freshwater input to the Labrador Sea in CESM1. (c) and (d) show that the surface heat flux anomalies are in the sense to drive a decline in AMOC, but the mixed layer depth decline leads the surface heat flux decline so the surface heat flux anomalies are more likely a response (or feedback) to the AMOC decline, rather than the trigger. (e) and (f) show that the decline in sea ice thickness precedes the mixed layer depth decline, suggesting sea ice decline is the more likely trigger of the AMOC than the other surface fluxes.

8
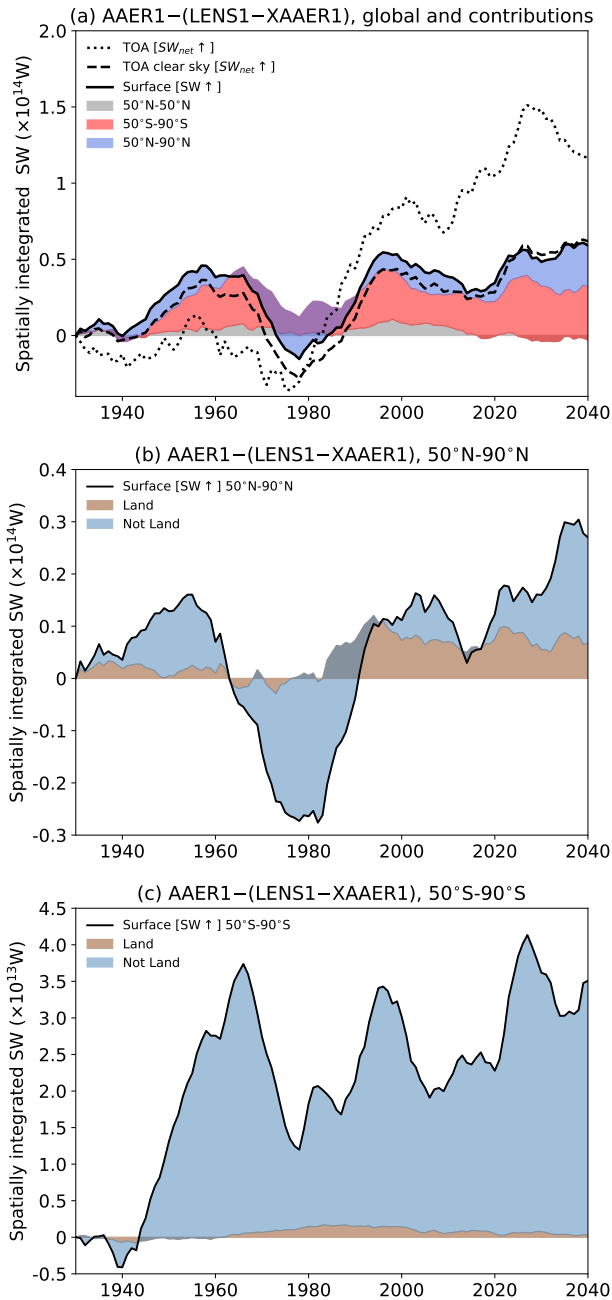
Fig. 11. As Figure 6 of the main text but for CESM1, showing the difference between AAER1 and LENS1−XAAER1 in the spatially integrated shortwave fluxes. (a) shows the global integral with black dotted showing the top of atmosphere net upward shortwave radiation and black dashed showing its clear sky component. Black solid shows the surface upward shortwave radiation and it is further divided into contributions from different latitude bands. (b) Surface upward shortwave radiation spatially integrated from 50°N to 90°N and the contributions from land regions and regions that are not land. (c) is as (b) but for 50°S to 90°S.

9
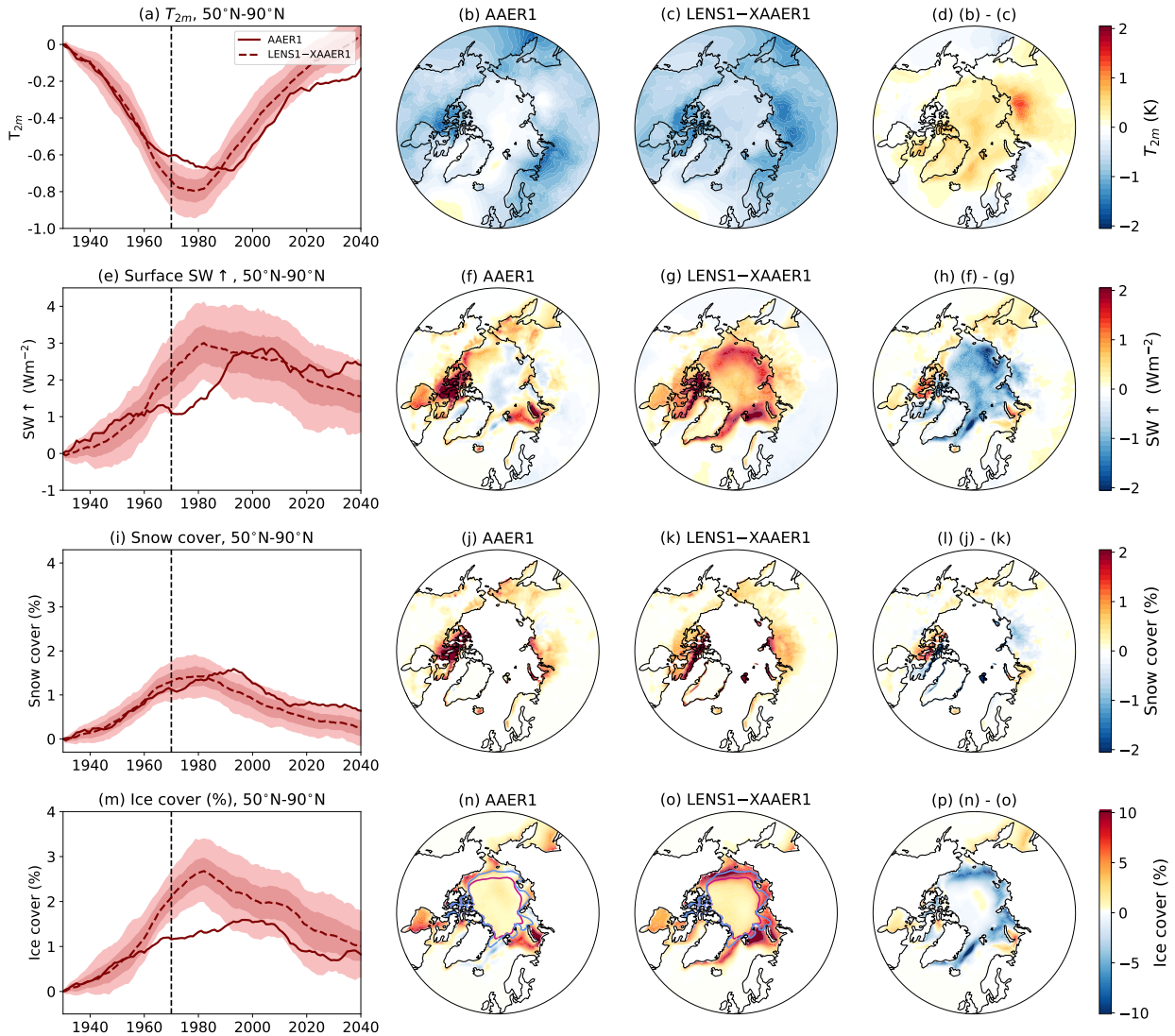
FIG. 12. As Fig. 7 of the main text but for CESM1. Aerosol influence on the JJA season from 50°N to 90°N. Left column shows time series of 21 year running means for (solid) the ensemble of AAER1 and (dashed) the ensemble mean of LENS1−XAAER1 anomalies from the 1920-1940 average. The dark and light shadings around the AAER1 line show the 95% confidence interval using (light shading) 3 members and (dark shading) 20 members of XAAER1. The dashed vertical line depicts 1970 (the center of the 1960-1980 period used for the anomalies shown in the right three columns). (2nd column) shows AAER1, (3rd column) shows LENS1−XAAER1 and (4th column) shows the difference between AAER1 and LENS1−XAAER1. (top) T_s, (2nd row) surface upward shortwave, (3rd row) grid cell area covered by snow in percent, (4th row) grid cell area covered by sea ice in percent. In (i) and (m) the 50°N-90°N average is taken only over land grid points and grid points that are not land, respectively.

10
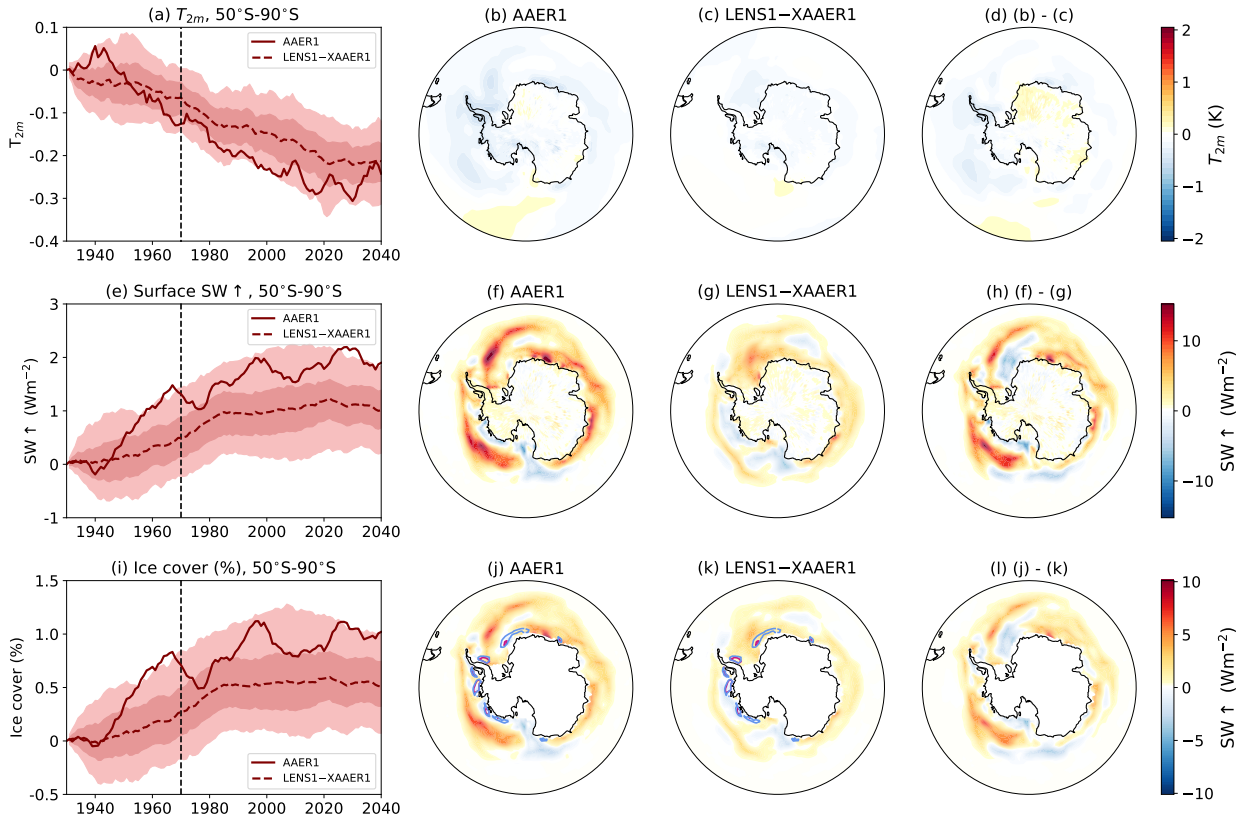
FIG. 13. As supplemental Fig 8 but for CESM1. (a)-(d) show DJF averaged near surface air temperature. (a) shows time series of 50°S-90°S average anomalies from 1920-1940. (b) Shows the anomalies for 1960-1980 for AAER1, (c) shows the anomalies for 1960-1980 for LENS1−XAAER1 and (d) shows the difference in anomalies between AAER1 and LENS1−XAAER1. (e)-(h) are as (a)-(d) but for surface upward shortwave radiation and (i)-(l) are as (a)-(d) but for the average percentage cover of sea ice in each grid point. The blue and purple contours in (j) and (k) show the 80% ice coverage contours for 1920 to 1940 of AAER1 and 1960 to 1980 of LENS1 respectively.
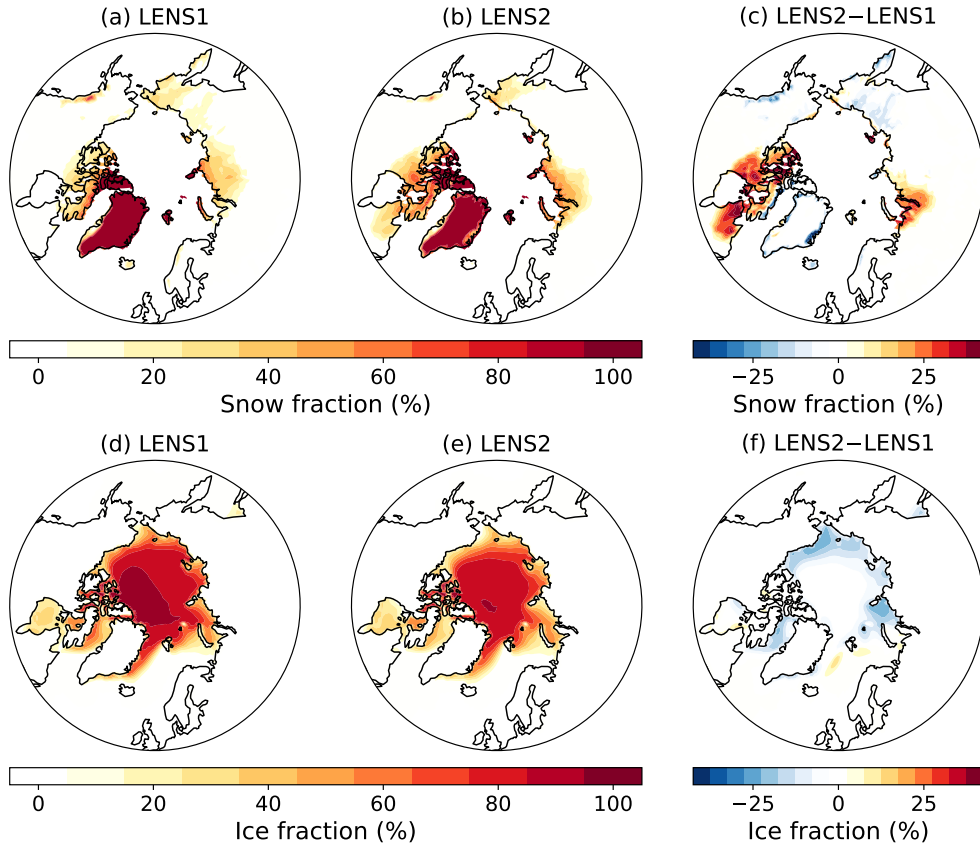
FIG. 14. Top shows the 1920-1940 JJA snow fraction climatologies for (a) LENS1, (b) LENS2, and (c) the difference between LENS2 and LENS1. Bottom shows the 1920-1940 JJA ice fraction climatologies for (c) LENS1, (d) LENS2, and (d) LENS2−LENS1.
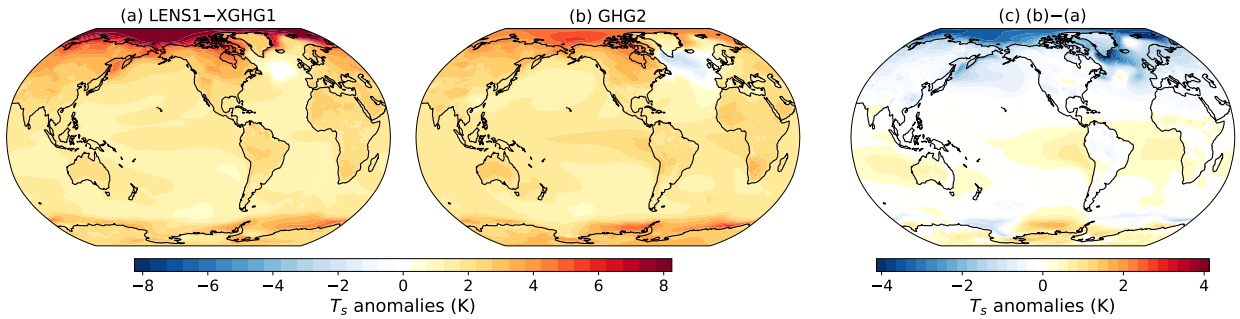

FIG. 15. 2030-2050 minus 1920-1940 near surface temperature anomalies due to greenhouse gases in (a) LENS1−XGHG1, (b) GHG2 and (c), the difference between GHG2 and LENS1−XGHG1.

References

Rodgers, K. B., and Coauthors, 2021: Ubiquity of human-induced changes in climate variability. *Earth Sys. Dynam.*, **12**, 1393–1411.